Noname manuscript No.
(will be inserted by the editor)

Wind Veer and Speed in Turbulent Ekman Flow Part I: Scaling analysis and universal profile model

Cedrick Ansorge[1] **and Hauke Wurps**[2,3]

Submitted November 13, 2024

Abstract
The profiles of wind speed and direction in turbulent Ekman flow are formulated based on asymptotic theory and data from direct numerical simulation. The profile of the streamwise component follows the classical viscous, logarithmic and wake scaling. In the outer layer, the velocity component profiles can be described by an Ekman-spiral with adapted boundary conditions that result in a reduction of the spiral-like rotation. The span-wise component poses a conceptual challenge to the channel-flow analogy in the context of asymptotic matching; it exhibits a mixed scaling in the surface layer, but follows outer scaling for most of the outer layer. Viscous stress scales universally across the boundary layer in inner units while the total stress becomes universal as a function of outer height. This implies a mixed scaling for the turbulent stress and eddy viscosity across the inner layer and convergence to a universal scaling as function of the outer height across the outer layer for increasing scale separation vide Reynolds numbers.

1 Introduction

The Coriolis force bends the apparent path of motion on a rotating sphere and establishes geostrophic equilibrium when in balance with a pressure gradient force. Wind veer away from the wind direction in geostrophic equilibrium is (i) due to direct frictional effects in the very vicinity of the surface and (ii) due to turbulence which exerts indirect frictional effects; these effects cause a slow-down of the mean wind reducing the Coriolis force thus turning the wind in favor of the pressure gradient force. Not only does the veering set the frame of reference for surface layer theory, it also has effects at small and large scales from large-scale dispersion via plume spreading to cyclone spin-down (Svensson and Holtslag 2009) and on the capabilities of data assimilation and accuracy of surface flux estimates (Brown

[1] FU Berlin, Institut für Meteorologie, Carl-Heinrich-Becker-Weg 6–10, 12165 Berlin, Germany
cedrick@posteo.de
[2] Carl von Ossietzky Universität Oldenburg, School of Mathematics and Science, Institute of Physics
[3] ForWind - Center for Wind Energy Research, Küpkersweg 70, 26129 Oldenburg, Germany

et al. 2005). From a large-scale perspective, the veering of wind across the planetary boundary layer determines the amount of cross-isobaric mass-flux, commonly referred to as 'Ekman pumping' (Ekman 1905), and it is thus a key factor in the life-cycle of large-scale synoptic systems. Within the atmospheric boundary layer (ABL), directional shear of the wind in the upper part of the surface layer may cause a systematic yaw for tall wind power generation devices where blades reach into the Ekman layer, i.e. that part of the boundary layer where the wind starts to turn; an exact estimate of such effects is critical in the site assessments for wind farms (Calaf et al. 2010; Mirocha et al. 2018).

In the planetary boundary layer, wind veer is characterized by the surface veering angle α defined as the angle between the negative surface shear stress τ_{sfc} and the geostrophic wind. Surface veering α and geostrophic drag $Z \equiv u_\star/G$, where the friction velocity $u_\star \equiv \sqrt{|\tau_{\mathrm{sfc}}|/\rho}$, uniquely determine the surface drag τ_{sfc} in a turbulent Ekman flow. In any quantitative description of the surface layer, the friction velocity $u_\star$ is the dynamic scale and α defines the horizontal alignment of the frame of reference, i.e. the rotation of the surface friction with respect to the outer wind direction. Knowledge about $u_\star$ and α is thus a prerequisite for any quantitative theory of the surface layer, and Rossby and Montgomery (1935) constrained the two parameters based on integral relations in the ABL. Asymptotic similarity theory was later used by Tennekes (1973); Blackadar and Tennekes (1968), and–based on his seminal direct numerical simulations (DNS) of Ekman flow–, Spalart (1989) suggested a modification to take into account effects of low to intermediate Reynolds numbers. Later on, constants were re-evaluated with a focus on the ABL based on observations (Högström 1988, 1996) and numerical modelling (Spalart et al. 2008, 2009; Ansorge and Mellado 2014; Ansorge 2019).

Attempts were also undertaken to obtain profiles of the wind speed: One approach is to match the inner and outer layer at a reference height as suggested by Etling (2002); Emeis (2018) (Sec. 21.10; Eq. 21.48); they choose the Prandtl-layer height z_{Prandtl} to match the wind speed profiles, which, however, requires external prescription of $\alpha(z_{\mathrm{prandtl}})$, the veering at that height. A one-dimensional profile with constant veering is given by Emeis et al. (2007, Sec. 3; Eq. 3.1-3.19).

Gryning et al. (2007) present an extension of the wind-speed profile beyond the surface layer using a neutral reference profile and a stability correction; Kelly and Gryning (2010), based on a probabilistic representation of stratification, develop a model for the long-term mean wind speed in the ABL and compare this with observation at different sites; Kelly and Troen (2016) demonstrate the effect of such improved model for wind-energy applications. In consideration of the large scale separation in geophysical flow, the rotation of the wind in the surface layer is often assumed negligible, and above investigations merely focus on the wind speed; that means, the veering of the wind with height is not described and there is little knowledge on the profile of the span-wise velocity component and the precise shape of the hodograph in the limit of a truly neutral Ekman boundary layer. A climatology of wind turning in the ABL is given by Lindvall and Svensson (2019) Klein et al. (2021) use a statistical turbulence modelling approach that yields a two-component velocity profile, but they also find that the exact representation of turning is challenging.

Ekman-layer models are roughly based on Ekman's seminal 1905 paper in combinations with additional assumptions. One option is a prescribed profile shape for eddy viscosity (Ellison (1955)), another are two-layer models of the ABL that take into account rotational effects at higher altitudes, for instance when the wind speed needs to be evaluated at heights on the order of $100 - 200\,\mathrm{m}$, a particular concern when it comes to wind-power forecasting (Etling 2002; Emeis 2018; Optis et al. 2014). Despite rotational effects being considered, the formulation of these models for the outer layer and analysis of their performance primarily focuses on wind speed. Still, in 2018, Jiang et al. recognized that the outer part of the Ekman boundary layer receives less attention in comparison with the surface layer and study the neutral problem by Large-Eddy simulation (LES). They focus on the wind speed and find an extended logarithmic layer when considering the wind speed instead of the shear-aligned component, and they eventually demonstrate by means of an analytical model that this vertical extension of the logarithmic layer may be explained by a transfer of stress to the span-wise velocity component where it is assumed that the shear vector $\tau(z)$ and stress vectors $(\partial_z U, \partial_z V)$ are aligned.

More recently, Ghannam and Bou-Zeid (2021) treated the horizontally averaged momentum budget to show that departures from shear-alignment in the vicinity of the surface result in an integral of the wind veer (α_M in their notation) over the height to very high accuracy ($\int_{z_0}^{H} \sin\alpha_M$ in their notation; their Eq. (16)). Classic surface-layer similarity is recovered when the angle α_M does not depend on height, i.e., the wind veer is constant across the surface layer. If, however, the wind veer depends on height, the profiles of stress and mean velocities depart from the scalings implied by classic surface-layer similarity.

Turbulent Ekman flow is considered here as a conceptual model of the homogeneous, stationary ABL over a flat surface under neutral stratification. Universal profiles of the wind vector for turbulent Ekman flow not only are a well-described limit for theoretical exploration or higher-order approaches taking into account possible effects of stratification, roughness or other physical complications encountered in the real geophysical system. While, on first sight, the study of such a strongly idealized case appears as an academic problem, it contains the essence of surface similarity as it is used in most atmospheric models, be it conceptual or numeric ones. More complex accounts generally refer to the homogeneous stationary problem as a base state: (i) Roughness is commonly incorporated by a linear transformation of vertical scale involving the roughness parameter z_0 and for larger roughness also a displacement height (Monin and Yaglom 1975; Jacobs and Van Boxel 1988; Högström 1988); (ii) Stability can be accounted for by a linearization around the neutrally stratified profile (Monin 1970; Monin and Yaglom 1975; Högström 1988, 1996; Sakagami et al. 2020); (iii) Non-stationarity in the pressure-gradient forcing can be accounted for by a linear damped-oscillator approach around the base state(Momen and Bou-Zeid 2016); (iv) Barotropic and baroclinic effects on the velocity profile require to consider the height-dependence of the veer and stress misalignment (Momen et al. 2018; Ghannam and Bou-Zeid 2021). Furthermore, such a solution can serve as better initial condition for numerical simulation of the flow, to minimize the length of initial transient periods, or as benchmark for turbulence closures that can be tuned to reproduce the neutral limit case.

Despite the strong simplifications implied by our choice of set-up, there is no straightforward approach to solving this well-defined problem. Large-Eddy simulation not only needs to be tuned for the surface shear stress and veering angle, but it also relies on sub-grid closures that commonly assume alignment of the turbulent stress with gradients. This pre-requisite is not fulfilled when the wind rotates with height. Esau (2004) investigated the representation of the Ekman boundary layer by dynamical subgrid closures and Zikanov et al. (2003) proposed a closure for the wind profile using a linearized representation of the eddy viscosity. Despite advances in analysis of this simplified set-up (Jiang et al. 2018), there is yet insufficient understanding for a quantitative generalization of the results to arbitrary external forcing (manifest in variation of the Reynolds number) – and indeed the fundamental questions pertaining to such relatively simple dynamics of turbulence are not reflected in the research on LES for the ABL over the past 50 years (Stoll et al. 2020).

At the same time, an increasing amount of high-quality and high-resolution data from turbulence-resolving approaches is emerging due to recent advances in high-performance computing and its application to geophysical problem sets; the geophysical range of scale separation, however, is–and it will remain so for the foreseeable future–out of reach for such simulation (Dimotakis 2005). Here, the routinely employed concept of Reynolds-number similarity can help. It postulates the existence of *fully developed turbulence* believed to occur for a sufficiently large but finite Reynolds number (Barenblatt and Goldenfeld 1995). (Already in 1998, this in fact lead Moin and Mahesh to the question *how high a Re is high enough*?) Certain statistics of fully developed turbulence, such as dissipation (Dimotakis 2005) or profiles of mean velocity (Barenblatt 1993), become independent of the Reynolds number when appropriately scaled; other statistics, such as the near-wall maximum in velocity fluctuation depend on Re (Baars and Marusic 2020) and externality of the flow may exert an impact on near-wall scaling (da Silva et al. 2014). It appears that for certain statistics in Ekman flow, fully-developed turbulence is reached with the Reynolds numbers that became possible due to an increase of computing capabilities over the past decades.

This paper exploits the robust features of mean velocity profiles from direct numerical simulation across a range of Reynolds numbers to formulate both the streamwise and span-wise components of the mean velocity vector as a function of the Reynolds number.

2 Problem formulation and numerical approach

We consider here incompressible, turbulent Ekman flow, that is, the turbulent flow over a flat rotating plate, as a physical model for the truly neutral ABL. The f-plane approximation is applied such that rotation only acts on horizontal velocity components; we thus neglect rotational effects on the horizontal components of velocity and dynamical effects due to latitudinal variation of the rate of rotation.

2.1 Notation and governing equations

The dimensional velocity vector of the numerical simulations is $\underline{U} = (U_1, U_2, U_3) = (U, V, W)$ over the coordinate system $Oxyz$, where an approximate alignment (plus/ minus few degrees) of the direction Ox with the surface shear stress is achieved. We consider velocity profiles only, i.e. all velocities are averaged over horizontal planes and in time, that is, they correspond to an Ensemble average. The coordinate Oz points away from the wall, and Oy points in the span-wise direction normal to Oxz. For analysis of the results, we use two coordinate systems that are (i) exactly aligned with the surface shear stress

$$\underline{\tau}_{\mathrm{sfc}} = \begin{pmatrix} \tau_x \\ \tau_y \\ \tau_z \end{pmatrix} = -\nu \left(\frac{\partial U}{\partial z} \hat{e}_x + \frac{\partial V}{\partial z} \hat{e}_y \right) \tag{1a}$$

and labelled by an upper index α as in $\underline{U}^{\alpha}$ for the velocity vector, and (ii) the coordinate system aligned with the free-atmosphere geostrophic wind labelled by an upper index G as in $\underline{U}^{G}$. We denote the square root of the modulus of surface shear, the surface friction, by

$$u_\star = \sqrt{|| - \underline{\tau}_{\mathrm{sfc}}||} \tag{1b}$$

and let $Z_\star = G/u_\star$; the surface veering angle $\alpha_\star$ is the angle between $\underline{\tau}$ and the geostrophic wind

$$\alpha_\star = \sphericalangle \left(\underline{G}, \underline{\tau}_{\mathrm{sfc}} \right). \tag{1c}$$

Analogously, we denote the height-local veering of the wind $\alpha(z) = \sphericalangle (\underline{G}, \underline{U}(z))$, where $\underline{G} = (G_1, G_2, 0)$ is the geostrophic wind vector.

We consider the incompressible Navier–Stokes equations for the three velocity components on the f-plane in a framework that is governed by (i) geostrophic wind magnitude $G = \sqrt{G_1^2 + G_2^2}$, (ii) Coriolis parameter f (representing the angular rotation), and (iii) kinematic viscosity ν. In absence of external variability, this system converges to a statistically steady state in the sense that flow statistics do not depend on time; and this state is defined by a Reynolds number, the only non-dimensional parameter that governs the system. We use the geostrophic wind as velocity and the Coriolis parameter f as time scale for the non-dimensional framework. This implies the Rossby radius $\Lambda_{\mathrm{Ro}} = G/f$ as length scale, such that one Reynolds number governing the problem reads as

$$\mathrm{Re}_\Lambda = \frac{G \Lambda_{\mathrm{Ro}}}{\nu}. \tag{2}$$

The scales used in defining Re_Λ are of limited relevance for description of the turbulent flow state. The turbulence scale separation in a wall-bounded flow is commonly characterized by the friction Reynolds number (Jiménez 2012):

$$\mathrm{Re}_\tau = \frac{u_\star \delta}{\nu} = \delta^+ = \frac{\mathrm{Re}_\Lambda}{Z_\star^2}, \tag{3}$$

where $\delta = u_\star/f$ and we use a superscript $'+'$ to denote normalization by inner turbulence scales $(u_\star, \nu)$. Another common measure of scale separation is the Reynolds number

$$\mathrm{Re}_D = \frac{GD}{\nu} \tag{4}$$

defined by the laminar Ekman layer thickness $D = \sqrt{2\nu/f}$.

The governing equations non-dimensionalized by G, f, and Λ_{Ro} read as

$$\frac{\partial u_i}{\partial t} = \frac{\partial \pi}{\partial x_i} - u_j \frac{\partial u_i}{\partial x_j} + \epsilon_{i2j}(u_j - g_j) + \frac{1}{\mathrm{Re}_\Lambda} \frac{\partial^2 u_i}{\partial x_j^2} \tag{5a}$$

$$\frac{\partial u_j}{\partial x_j} = 0, \tag{5b}$$

where $u_i = U_i/G$ are the non-dimensional components velocity, π is non-dimensional pressure, $g_j = G_j/G$ are non-dimensionalized components geostrophic wind (with $g_1^2 + g_2^2 = 1$ by construction), and ϵ is the Levi–Civita tensor. These equations are solved inside a bounded cube of size $L_x \times L_y \times L_z$ with periodic boundary conditions in the lateral (streamwise and spanwise) directions, a no-slip–no-penetration boundary at $z = 0$, and a no-penetration, free-slip boundary at $z = L_z$.

2.2 Numerical simulations

The problem is solved numerically by tLab[1], an open-source tool-suite to simulate and analyze turbulent flows. We use here a fourth-order–five-step Runge–Kutta integration and sixth-order compact schemes for spatial derivatives in all directions. The incompressibility constraint is enforced by a fractional step approach where the Poisson equation for the pressure field is solved to machine accuracy using a combined spectral/compact approach as described in Mellado and Ansorge (2012).

Simulations used here are shown in Tab. 1. We extend an existing set of simulations for $\mathrm{Re}_\Lambda \in \{125\,000; 281\,250;\ 500\,000\}$ (gray shading; cf. Ansorge and Mellado 2014, 2016) by new simulations at higher Reynolds numbers up to $\mathrm{Re}_\Lambda = 1.28 \times 10^6$ with a horizontal domain extent up to 3.3×10^4 viscous units. In total, this yields one order of magnitude variation in terms of the scale separation in the boundary layer.

3 Scaling behavior of the flow for Re_τ up to 3000

The generalization of profiles to arbitrary Reynolds numbers requires sufficient scale separation in the simulations, not only to quantify the effect of the Reynolds number on low-order flow statistics, but also to assess the corresponding rate-of-change to eventually allow for an extrapolation of the findings. While the simulations previously available (gray shading in Tab. 1) give confidence in a first-order representation of the turbulent problem, the estimation of higher-order effects such as the dependency of the Reynolds number requires a broader scale separation that is made available by the two new simulations at increased Reynolds number (cf. Tab. 1). Data at such scale separation has been obtained previously (cf. Spalart et al. 2008, 2009), but we also need high confidence with respect to the convergence of simulation data for slow oscillations and with respect to sampling convergence, which translates to two further requirements on the data: First, data should be free

[1] https://github.com/turbulencia/tlab

Table 1 Direct numerical simulation data sets used in this work. Re_Λ and Re_D refer to the Reynolds number defined in terms of the Rossby radius Λ and Ekman-layer thickness D respectively. L_{xy} is the domain size in the stream- and span-wise direction. The grid is given by the number of grid points in the stream-wise (N_x), span-wise (N_y) and vertical (N_z) directions respectively. The resolution in the span-wise and stream-wise directions are given as Δx^+ and Δy^+. The grid in the vertical is stretched, and resolution at the wall is given by Δz^+.

Re_Λ	Re_D	L_{xy}/Λ	$N_x \times N_y \times N_z$	Δx^+	Δy^+	$\Delta z^+\|_{z=0}$
125 000	500	1.08	$2048 \times 2048 \times 192$	4.1	4.1	1.05
281 250	750	1.08	$3072 \times 3072 \times 384$	5.6	5.6	1.60
500 000	1 000	1.08	$3072 \times 6144 \times 512$	9.3	4.7	1.14
845 000	1 300	0.54	$2560 \times 5120 \times 640$	8.9	4.5	0.99
1 280 000	1 600	0.54	$3860 \times 7680 \times 960$	8.6	4.3	1.00

Table 2 DOIs and reference to the openly accesible data set at refubium repository

Re_D	DOI	Reference
500	10.17169/refubium-42505	Ansorge (2024a)
1000	10.17169/refubium-42507	Ansorge (2024b)
1300	10.17169/refubium-42508	Ansorge (2024c)
1600	10.17169/refubium-42509	Ansorge (2024d)

of artifacts from long-term oscillations across the vertical extent of the domain–primarily, simulations should be free of effects originating from the inertial oscillation; this is achieved here by replacing the mean value of the three-dimensional velocity fields by the time mean over a whole inertial oscillation. Second, high accuracy is also needed in terms of the statistical convergence of averages, bulk measures and large-scale structures; this requires a domain size $L_x > \mathcal{O}(\delta_{95})$. We use here $L_x = L_y = 1.08\Lambda$ for cases with $\mathrm{Re} \leq 1000$ and $L_x = L_y = 0.54\Lambda$ for $\mathrm{Re} \geq 1300$ which corresponds to $L_x/\delta_{95} \approx 25$ for $Re_D = 500$ and $L_x/\delta_{95} \approx 18$ for $Re_D = 1300$.

Bulk parameters of the simulations are given in Tab. 3. The surface stress is characterized by $u_\star$ and $\alpha_\star$ in relation to the geostrophic wind vector and discussed in more detail as the drag law below in Sec. 4.1 (we find the expected slight decrease of $u_\star/G$ and $\alpha_\star$ with increasing Re). The boundary-layer height estimated from the 95% stress reduction, δ_{95}, is around 0.6δ to 0.66δ. Interestingly, the integrated TKE $\int_0^\delta e \mathrm{d}z$ stays constant when normalized by the friction velocity $u_\star$ while the integrated dissipation $\int_0^\delta \epsilon \mathrm{d}z$ exhibits inviscid scaling when normalized by the magnitude G of the geostrophic wind. (TKE and dissipation normalized as $fG^{-3}\int e\mathrm{d}z$ and $u_\star^{-3}\int \epsilon \mathrm{d}z$, exhibit substantial dependence on Re for the variation of $u_\star$.) This indicates that the bulk dissipation is governed by the forcing G–irrespective of Re. Changes in Re, however, affect the level and organization of turbulence, and the parameter representing this dependency is the friction velocity $u_\star$ which describes the turbulence production processes in the surface layer, in particular in the buffer layer.

Velocity profiles in inner units ($U^{\alpha+}(z^+)$, Fig. 1a)and outer units ($U^{\alpha-}(z^-)$, Fig. 1b) are in accordance with previous work (Coleman et al. 1992; Spalart et al. 2008, 2009; Ansorge and Mellado 2014; Ansorge 2019): The profiles of the shear-aligned streamwise velocity component are well-collapsed for $\mathrm{Re}_D > 500$ below $z^- \approx 0.15$ (circles in Fig. 1a); the case with $\mathrm{Re}_D = 500$ is only transitionally

Table 3 Bulk characterization of the simulations for different Reynolds numbers Viscous Reynolds number Re, friction Reynolds number Re_τ, friction velocity $u_\star$, surface veering angle $\alpha_\star$, normalized boundary layer depth δ_{95}/δ, inner normalization of vertically integrated TKE, outer normalization of vertically integrated dissipation.

Re	$\delta^+ = \mathrm{Re}_\tau$	$u_\star/G$	$\alpha_\star$	δ_{95}/δ	$fu_\star^{-3}\int_0^\delta e\mathrm{d}z$	$G^{-3}\int_0^\delta \epsilon\mathrm{d}z$
500	479	0.0619	25.5	0.66	0.88	1.31
750	886	0.0561	21.0	0.65	0.90	1.34
1000	1403	0.0530	18.8	0.62	0.92	1.30
1300	2122	0.0501	17.9	0.59	0.85	1.24
1600	2978	0.0482	17.2	0.61	0.91	1.21

turbulent and there is no distinct inner-outer scale separation. The logarithmic law is appropriate for $50 < z^+ < 0.15Re_\tau$, where $z^+ = Re_\tau z^-$. While the profiles $U^{\alpha_\star +}(z^+)$ diverge between different Re beyond $z^- = 0.15$, the corresponding profiles of the velocity deficit $(U^{\alpha_\star}(z^-) - G_1^\alpha)/u_\star$ agree closely, irrespective of Re. This illustrates the inner–outer scale-duality in this external flow with inner scaling being appropriate in the inner layer and outer scaling in the outer layer. Also in the outer layer of the flow, $u_\star$ (and not the magnitude of the geostrophic wind G) governs the inviscid normalization, i.e. a scaling independent of the Reynolds-number.

No collapse is found for the profiles of spanwise velocity when considered in inner units, $V^{\alpha_\star +}(z^+)$. When normalized in outer units, the deficit profiles of spanwise velocity $(V^{\alpha_\star}(z^-) - G_2^\alpha)/u_\star$ agree well beyond $z^- \approx 0.3$. This is a much higher level in comparison with the streamwise component that collapses also within the overlap layer, i.e. much closer to the surface (circles in Fig. 1b). The value of $V^{\alpha_\star +}(z^-) - G_2^\alpha$ is sensitive to the wind veering for $z \to 0$ as—for use of the shear-aligned component—it has to approach the value $-G_2^\alpha = |G|\sin\alpha \neq 0$ in view of the no-slip boundary condition. While low-Re effects appear to be present for $\mathcal{O}(\mathrm{Re}) < 10^3$, the spanwise component converges to an Re-independent limit within the range of scale separation considered here, i.e.

$$G_2^\alpha/u_\star = Z_\star \sin\alpha \to \text{const. for Re} \to \infty, \tag{6}$$

which has indeed already been found by Spalart (1989), who estimates the constant from an integral relation.

The viscous stress

$$S_{\mathrm{visc}} = \nu\sqrt{\left(\frac{\partial U}{\partial z}\right)^2 + \left(\frac{\partial V}{\partial z}\right)^2} \tag{7a}$$

exhibits universal scaling when considered as $S^+_{\mathrm{visc}}(z^+)$ (Fig. 2a); this normalization is also appropriate in the outer layer where the viscous stress is, however, small. Small deviations from the universal profile are observed for the smallest Reynolds number $\mathrm{Re} = 500$; we attribute these to low-Re effects in the only transitionally turbulent flow ($\mathrm{Re}_\tau = 479$). In contrast to the viscous stress, the total stress follows outer normalization, i.e. $S^+(z^-)$ is universal; a discrepancy in the inner layer does not occur as the total stress is approximately constant in the viscous and buffer layer, and a rescaling of the height would have no effect there;

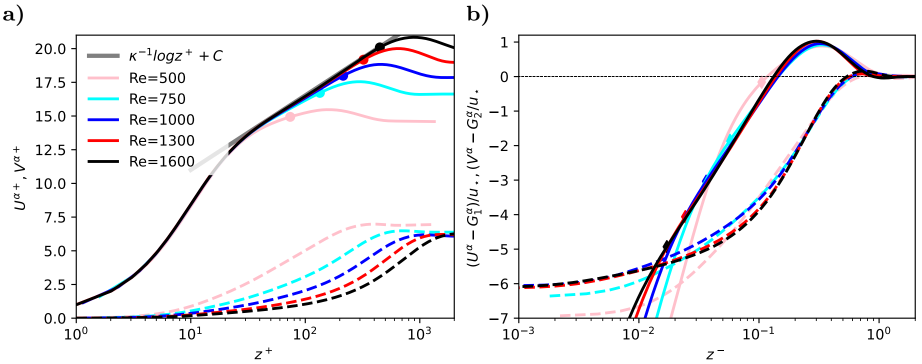

Fig. 1 **a)** Shear-aligned velocity profiles in inner units; circles mark the height $z^- = 0.15$; **b)** Shear-aligned velocity deficit in outer units; diamonds mark the grid point closest to the height $z^+ = 50$

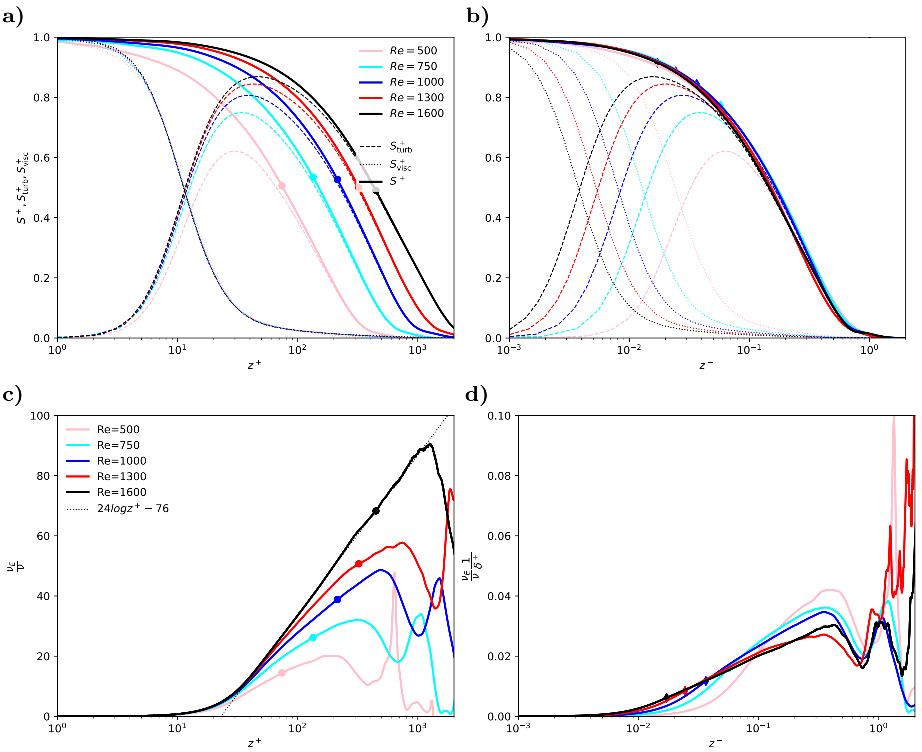

Fig. 2 **a-b)** Profiles of the turbulent stress $S^+_{\rm turb}$ (dashed), the viscous stress $S^+_{\rm visc}$ (dotted), and the total stress, $S^+ = S^+_{\rm visc} + S^+_{\rm turb}$ (solid) as a function of inner height **(a)** and outer height **(b)**. **c-d)** Normalized eddy viscosity ν_E (solid) plotted versus inner height **(c)** and outer height **(d)**. **(c)** uses inner normalization; **(d)** uses normalization by $\nu\delta^+$ which approximately collapses data in the outer layer. Different colors are for different Reynolds numbers (cf. Tab. 1). Circles in **(a)** and **(c)** denote the height $z^- = 0.15$, diamonds in **(b)** and **(d)** are for $z^+ = 50$ as in Fig. 1

above, outer scaling is appropriate for the well-established dynamics in the overlap region of inner and outer layer. This, however, implies a mixed scaling for the turbulent stress,

$$S_{\mathrm{turb}} = \sqrt{\overline{u'w'}^2 + \overline{v'w'}^2}, \tag{7b}$$

where dashed quantities u', v', w' indicate deviations from the mean and the overbar denotes horizontal and time averaging. Indeed, S_{turb} only follows inner normalization below $z^+ \lesssim 20$ (where the turbulent contribution is negligible). In the outer layer, where $S_{\mathrm{visc}} \to 0$, S^+_{turb} follows outer normalization for $z^- \gtrsim 0.15$—with increasing accuracy for larger Re and larger distance from the surface. In the overlap region, i.e. for $z^+ > 20$ and $z^- < 0.15$, the mixed scaling for the turbulent stress can be expressed as

$$S^+_{\mathrm{turb}}(z^+, \mathrm{Re}_\tau) = S^+(z^-) - S^+_{\mathrm{visc}}(z^+), \tag{7c}$$

where $z^- = z^+/\mathrm{Re}_\tau$.

The Eddy viscosity plays a crucial part when modelling profiles and the vertical transport in turbulent flow. In analogy to the Fick-law for molecular diffusion, the eddy diffusivity is the effective diffusivity that yields the turbulent transport S_{turb} based on the strain rate. For the symmetries in the flow (horizontal homogeneity, and $W = 0$), it is

$$\nu_E = \frac{S_{\mathrm{turb}}}{\sqrt{\left(\frac{\partial U}{\partial z}\right)^2 + \left(\frac{\partial V}{\partial z}\right)^2}} = \nu \frac{S_{\mathrm{turb}}}{S_{\mathrm{visc}}}. \tag{8a}$$

The inner normalization of ν_E is obtained when dividing by the molecular viscosity:

$$\nu_E^+ = \nu_E/\nu = S_{\mathrm{turb}}/S_{\mathrm{visc}}. \tag{8b}$$

Under this normalization, the profiles of eddy viscosity collapse below $z^+ \approx 20$ with a tendency towards better collapse at higher z^+ for higher Reynolds number (up to $z^+ \approx 50$ for Re = 1600; Fig. 2c). In the outer layer, the eddy viscosity is characterized by a distinct minimum at $z^- \approx 0.6 - 0.8$, and we find that the following mixed normalization of ν_E by the geostrophic wind and friction velocity collapses the value of ν_E at this minimum (cf. Fig. 2d):

$$\nu_E^- = \nu_E^+ \frac{1}{\delta^+} = \nu_E \frac{1}{\nu} \frac{\nu}{u_\star \delta} = \nu_E \frac{f}{u_\star^2}. \tag{8c}$$

Substantial variation of the profiles is, however observed below and above this minimum for different Re which illustrates that this normalization is probably not generally appropriate across the outer layer.

The organization of the flow with $Re_\tau = 2978$ is depicted in terms of the turbulence kinetic energy in Fig. 3. In vicinity of the wall, at $y^+ \approx 10$, (Fig. 3a), elongated streaks aligned with the surface shear stress dominate. Moving away from the wall, to $y^+ \approx 150$ (well within the logarithmic region), the structures are larger and more isotropic, but they are still largely aligned with the surface shear stress. In the upper part of the outer layer, around $y^+ \approx 1000$, no clear signature of the surface veering direction is found, and intense TKE structures (bright yellow) are organized on a large spatial scale with weaker eddies (greenish structures) and quiescent regions in between.

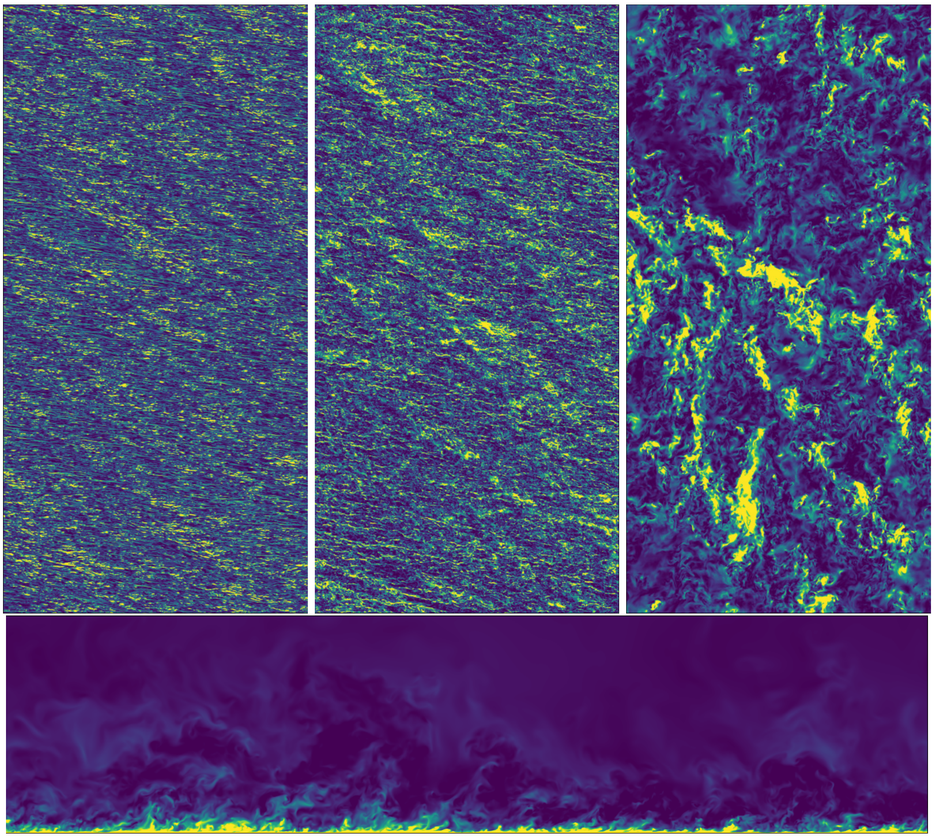

Fig. 3 Horizontal slices of turbulence kinetic energy in the Buffer layer (i=10), logarithmic Layer (i=100), and outer layer (i=400) of the case with $Re_\tau = 2978$; coloring between percentiles 4 and 96 of the respective image. Lower panel:streamwise–vertical intersect through the domain

4 A universal velocity profile for the turbulent Ekman layer

We now turn to the formulation of a general velocity profile that is fully determined by the only parameter of the idealized problem, namely a Reynolds number representing the scale separation or geometric size of the problem. This precludes, first, a drag law wherewith we begin this section (4.1). Based on the scaling arguments put forward in Sec. 3, we then develop, second, a formulation of the wind vector in the Ekman layer (Sec 4.2). Finally, we come up with a separate formulation of the, third, stream-wise and, fourth, span-wise velocity components in the overlap and inner regions of the flow.

4.1 Drag-law

A drag-law for Ekman flow determines—as a function of Reynolds number alone—the surface drag. This can be formulated by the normalized surface friction, $u_\star$

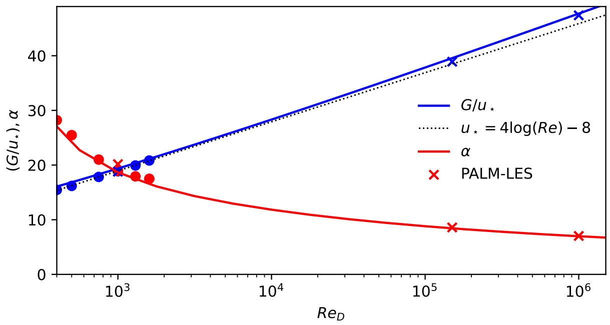

Fig. 4 Variation of geostrophic drag, $Z_\star$, and surface veering, $\alpha_\star$, with Reynolds number according to the theory by Spalart et al. (1989) and as estimated from DNS data

(Eq. (1b), also termed geostrophic drag), and the direction of surface shear stress, $\alpha_\star$ (Eq. (1c), also termed wind veer). A non-zero veering of the wind is a rather special case in comparison with most turbulent flows considered in an engineering context, and it confronts us with a situation where the most appropriate coordinate system for analysis (namely that aligned with the surface shear stress) is a priori unknown. We compare our DNS data against a semi-empirical drag-law based on integral consideration (Spalart 1989) and find, as demonstrated in previous work (Ansorge and Mellado 2014), excellent agreement in the range $400 < \mathbf{Re} < 1600$, representing a factor of 16 in variation of viscosity.

We also find that the solution of the transient equation involved in estimation of $u_\star$ for a given Reynolds number Re_D is approximated reasonably by the formulation

$$Z_\star = 4\log(\mathbf{Re}_D)) - 8 \tag{9}$$

which quantifies the 'weak' dependence of $u_\star$ on the Reynolds number as an approximately logarithmic one, at least for problems with a scale separation on the order that is relevant to geophysical problems ($Re_D < 10^8$).

4.2 Profile in the Ekman layer

Formulations for the outer layer that take into account the rotation (and thus deviation from the channel-flow analogy) need to be matched to the framework of surface similarity. A smooth transition from the inner layer to the Ekman layer, where the wind is characterized by a turning of its mean direction, is not easily achieved. Optis et al. (2014), for instance, define an *"effective geostrophic wind vector that has the same magnitude of the observed surface geostrophic wind and is rotated by the angle α [their nomenclature]"* to overcome the unsteady transition when approaching the Ekman layer from below. Such rotation of the wind vector is *a posteriori* justified by the observational data that the model outcomes are compared to. This need for a connection of the two reference frames is a manifestation of a mismatch in the theoretical treatment of the inner and outer layer in this rotating flow configuration.

The text-book solution for Ekman flow makes use of the physical boundary conditions (BCs) for the ABL (no-slip at the bottom and geostrophic wind in the

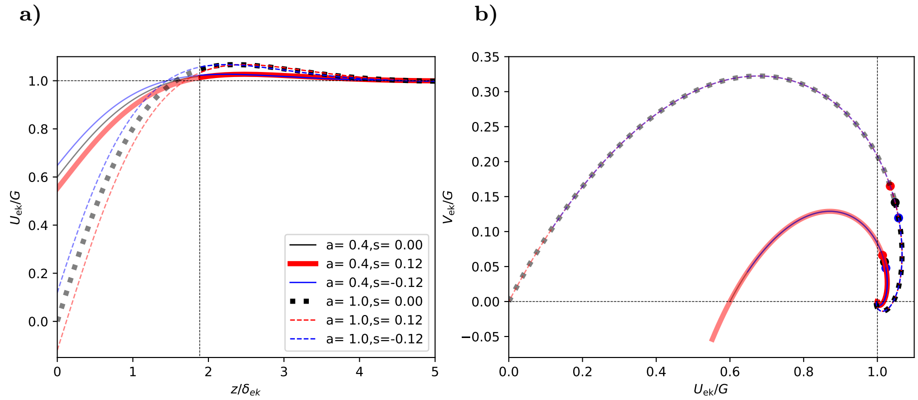

Fig. 5 **a)** Generalized Ekman-profile of the geostrophic-aligned component U_{ek}. **b)** Hodograph for the geostrophic-aligned and pressure-gradient aligned components U_{ek} and V_{ek}. Thick, black dashed line shows the classic solution. The height corresponding to $z^- = 0.30$ is marked by the dashed line in panel **(a)** and by filled circles in panel **(b)**. The hodograph and profiles above this reference height are shown as solid lines, below as opaque line.

free atmosphere) and a constant eddy viscosity. Specifying the boundary conditions at top and bottom eliminates one mode of the analytical solution, and it determines the magnitude of the spiral. In doing so, one has to assume that the solution is appropriate across the entire ABL, which is not the case: The dynamics put forth by Ekman in 1905 are not appropriate in the surface layer of the ABL; better approximations exist for the logarithmic, buffer, and viscous sublayers. In view of this situation, we use an adapted Ekman spiral that does not enforce the boundary conditions at the surface but at a different height. This is achieved by considering the Ekman spiral only in the Ekman layer, thus giving way for the well-established logarithmic and viscous-layer profiles in the lower surface layer. Based on the derivation in App. A.1, this profile is given by

$$\frac{1}{G}\begin{pmatrix} U_{\mathrm{ek}} \\ V_{\mathrm{ek}} \end{pmatrix} = \begin{pmatrix} 1 \\ 0 \end{pmatrix} + e^{-z_{\mathrm{ek}}}\left[a_{\mathrm{ek}}\begin{pmatrix} -\cos z_{\mathrm{ek}} \\ \sin z_{\mathrm{ek}} \end{pmatrix} + b_{\mathrm{ek}}\begin{pmatrix} \sin z_{\mathrm{ek}} \\ \cos z_{\mathrm{ek}} \end{pmatrix}\right]. \tag{10a}$$

with $z_{\mathrm{ek}} = \delta_{\mathrm{ek}}(z^- - s_{\mathrm{ek}})$. The right-hand-side consists of two modes with magnitude a_{ek} and b_{ek} shifted by $\pi/2$ with respect to each other. In the classic case, the second mode governed by b_{ek} is incompatible with the surface boundary condition. While this is not the case here for the general form of the profile, the phase shifts can also be captured by the parameter s_{ek}, and we stick with to a single-modal approach, i.e., we let $b_{\mathrm{ek}} = 0$.

This single-modal solution is characterized by three parameters, (i) an Ekman-layer depth scale δ_{ek}, (ii) the magnitude parameter of the spiral a_{ek}, and (iii) a zero-crossing point for the velocity s_{ek}. The effects of varying these parameters are illustrated in Fig. 5 where the classic Ekman solution is recovered by setting $a_{\mathrm{ek}} = 1$, $s_{\mathrm{ek}} = 0$ and $\delta_{\mathrm{ek}} = \sqrt{2\nu/f}$. These parameters are *a priori* unknown as they need to conform to the turbulent state of the boundary layer; we use our DNS data to arrive at best estimates for them.

The Ekman-layer depth scale δ_{ek} is fundamentally defined by the eddy viscosity. However, we have seen in Section 3 that a characteristic value for the eddy diffusivity is not easily obtained for its strong dependence on the Reynolds number and distance from the surface. We therefore resort to the physical manifestation of the eddy diffusivity in an Ekman layer, and use the boundary layer depth $\delta_{\mathrm{ek}} = 0.66\delta \times 2\pi$. For the relation $\delta_{\mathrm{ek}} = \sqrt{2\nu_{\mathrm{ek}}/f}$, this yields $\nu_{\mathrm{ek}} \propto u_\star^2/f$ in accordance with the observations in Sec. 3 (Eq. 8c).

The magnitude parameter of the Ekman spiral, a_{ek}, defines the super-geostrophic maximum of the wind profile aloft the logarithmic layer. Our simulations suggest this maximum of the velocity deficit remains constant when normalized by $u_\star$ as shown in Fig. 6. The numerical value of a_{ek} is estimated from visual comparison, and we find $a_{ek} = 8.4u_\star$; while this appears rather large, it is pre-multiplied by $e^{-z_{\mathrm{ek}}}$ which has already decreased to $\mathcal{O}(0.1)$ at the height of this maximum. This choice ascertains that the velocity deficits $U/u_\star - Z_\star$ and $V/u_\star - Z_\star$ do not depend on the velocity scale $u_\star$, but only on G as

$$U_{\mathrm{ek}}/u_\star - Z_\star \propto a_{\mathrm{ek}} Z_\star = 8.4G. \tag{11}$$

The offset parameter s_{ek} defines the zero-crossing height of the profile (in contrast to δ_{ek}, which determines the thickness across which the wind veering takes place). Physically, this offset can be understood as the height at which the surface was located assuming a perfect Ekman flow down to the surface. As this is not the case, and gradients are steeper in the highly turbulent boundary layer flow encountered when approaching the surface, the offset is smaller than zero (the fully turbulent boundary layer is actually thinner than an Ekman layer would be). From our DNS data, we estimate $s_{\mathrm{ek}} = -0.12$.

In summary, the outer layer of Ekman flow is characterized by a turning of the wind velocity and the super-geostrophic maximum that is sustained by momentum convergence at the inflection point of the velocity profile. The super-geostrophic maximum of streamwise velocity and a secondary minimum aloft the bulk-turbulent part of the boundary layer are well-described by a classic Ekman spiral with adapted boundary conditions and a shift in reference height. Corresponding profiles are shown in comparison with data from three DNS runs in Fig. 6. The idealized profiles capture the secondary minimum and convergence to the geostrophic equlibrium in the non-turbulent flow very well.

4.3 Streamwise velocity component

Well-established theories exist for the streamwise velocity profile, which in non-rotating flows is aligned with the surface shear stress due to the geometry. These theories cover various regimes based on their distance from the wall and the relative influence of viscosity, turbulence, and interaction with the outer flow region, with the logarithmic law for the mean velocity serving as a central reference point.

In immediate vicinity to the surface, local turbulent mixing cannot occur for the no-slip/no-penetration boundary condition, and the mean velocity is described by a viscous profile of the form

$$U^{\alpha_\star +} = z^+ \tag{12a}$$

where the direction of the velocity points into the exact opposite direction of the wall shear stress τ. In absence of roughness elements and for small roughness

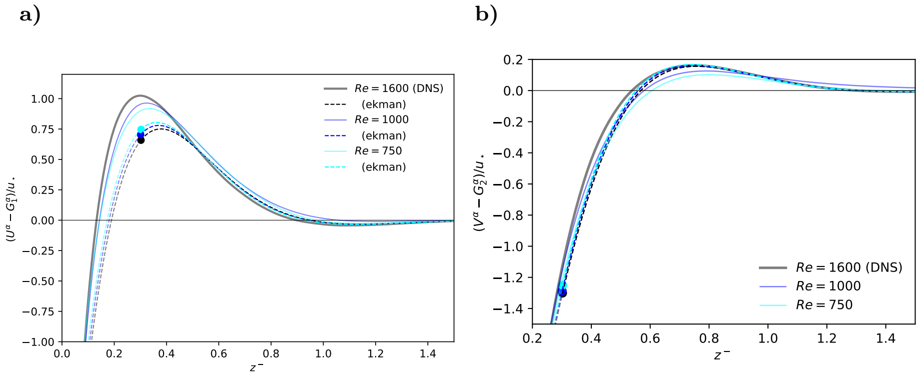

Fig. 6 Shear-aligned velocity deficit for the streamwise (panel **(a)**) and spanwise (panel **(b)**) components of the mean velocity U^{α} and V^{α}. Solid lines show DNS data, dashed lines the Ekman profiles U_{ek} and V_{ek} as defined in Eq. 10. Variations in U_{ek} and V_{ek} are a consequence of the normalization and related to changes in $u_\star$ and $\alpha_\star$ among the different Re_D.

($z_0^+ < 5$), this linear regime is known as viscous sub-layer Foken (2002); Foken et al. (1978). In fact, this law of the wall has no degree of freedom given the drag, i.e. once $u_\star$ and $\alpha_\star$ are defined. However, theoretical foundation is lacking for the exact shape of the velocity profile in the buffer layer; though crucial for turbulence production, it is commonly understood as a transition region between the linear profile at the surface and the logarithmic profile aloft. A pure blending from the linear velocity profile into the logarithmic one is, however, not reasonable as both the linear and logarithmic profile overestimate the velocity in the buffer layer. We therefore introduce a two-step correction procedure, accounting for the smaller-than linear growth beyond $z^+ \approx 5$, and assuring smooth matching with the logarithmic law at $z^+ = 40$:

$$U_{\mathrm{inner}}^{\alpha_\star +} = \frac{z^+}{1 + c_1 (y^+)^2} + (c_2 z^+ - a_{\mathrm{match}}) \frac{1 + tanh\left[0.2(z^+ - 22)\right]}{2} + c_3 e^{-c_4 (z^+ - 22)^2}. \tag{12b}$$

We use here

$$c_1 = 0.00185; \quad c_2 = 0.195; \quad c_3 = 0.4; \quad c_4 = 0.35.$$

The second and third terms on the right hand side vanish for $z^+ \ll 22$, and $c_1 = 0.00185$ implies an approximately 5% correction at $z^+ = 5$ and an 18.5% correction at $z^+ = 10$. The second and third term on the R.H.S. of eq. (12b) are an empirical fit to the velocity profiles observed in the buffer layer and appear independent of the Reynolds number for the range observed here. The coefficient a_{match}, which has no effect in the viscous sublayer, is then used to match this formulation to the logarithmic law employed above.

In the logarithmic region, we use the profile

$$U_{\log}^{\alpha_\star +} = \frac{1}{\kappa} \log z^+ + C \tag{12c}$$

with the von-Kármán constant $\kappa = 0.416$ and the boundary condition $C = 5.4605$. For this logarithmic law, $a_{\mathrm{match}} = 3.569861$ for a matching at $z^+ = 40$.

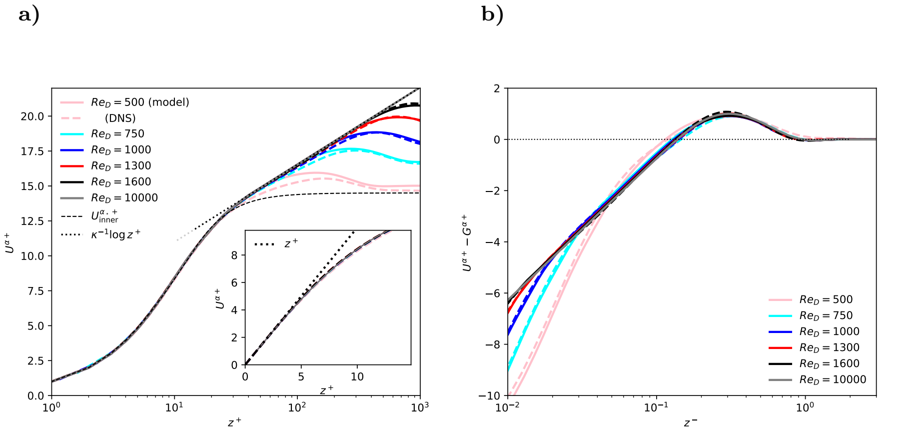

Fig. 7 Shear-aligned profiles of velocity components $U^{\alpha_\star+}$ in inner (left) and outer (right) units.

4.4 Spanwise velocity component

The background rotation and associated veering of the surface wind implies a non-zero profile for the span-wise velocity which challenges the conventional assumptions related to the channel-flow analogy: While the analogy with channel flow in vicinity of the wall implies that the streamwise component be zero or at least small, the veering requires a value of $V_{top} = U_G \sin\alpha_\star$ in the free stream (and thus also at the top of the boundary layer if we assume that any substantial velocity gradient is confined to the turbulent part of the flow). This continuous rotation of the wind vector is conveniently visualized by velocity hodographs aligned with the outer, geostrophic flow (cf. Fig. 5b) and normalized by the geostrophic wind. The geometry of the flow and its drag imply the following for any hodograph: (i) the boundary conditions at the surface, (ii) the boundary condition at the top, and (iii) the inclination of the hodograph at the origin by the surface veering:

$$V^{\alpha_\star}(z=0) = 0, \tag{13a}$$

$$\lim_{z\to\infty} V^{\alpha_\star} = G\sin\alpha_\star \tag{13b}$$

$$\partial_{z^+} V^{\alpha_\star +}\big|_{z=0} = 0. \tag{13c}$$

Outer scaling of the velocity profile further implies that the velocity deficit of $(V^{\alpha_\star} - G^{\alpha_\star})/u_\star$ be a universal function of the outer height z^-. In the outer region of the flow (for $z^- \mapsto 1$), $f_V(z^-)$, should govern the spanwise velocity profile, as is supported by our DNS data (Fig.1b); above $z^- \approx 0.3$, this profile is very well approximated by the Ekman-turning derived above (Eq. (10); Fig. 6b). While this deficit is a signature of outer rotation, it is inappropriate to extend this general relation to the surface where inner scales matter: On the one hand, the variation of the spanwise velocity deficit across the boundary layer (i.e. between $0 < z^- < 1$) must match the difference implied by the drag law $(u_\star, \alpha_\star)$ and the constant value of $V^{\alpha_\star}$ around $z^- = 0.3$. On the other hand,–provided the outer velocity deficit is Re independent–the Re-dependence of $\alpha_\star$ and $u_\star$ implies that this difference cannot be constant as a function of Re. We hence ask, how does the

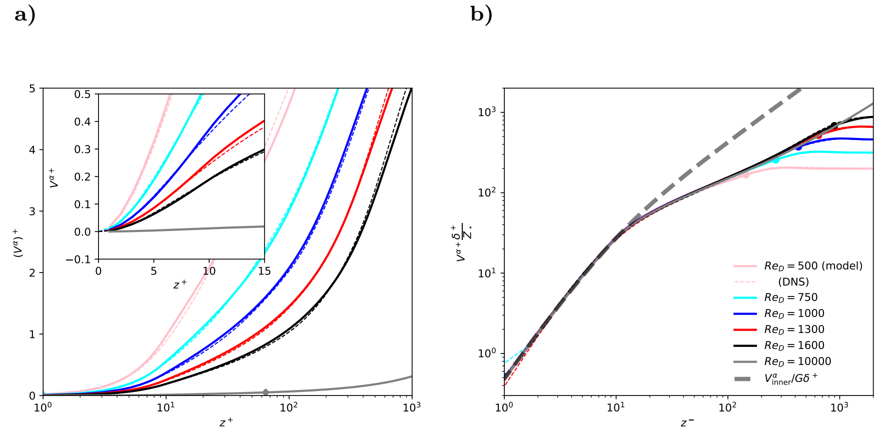

Fig. 8 Profiles of shear-aligned span-wise velocity $(V^\alpha)^+$ versus inner height. Dashed lines show DNS data, thick, opaque lines are from the semi-emprical theory developed above. Panel **(a)** shows standard inner normalization, panel **(b)** the inviscid normalization yielding a universal profile for the spanwise component of velocity in the inner layer.

span-wise component scale when the surface is approached? Clearly, the spanwise contribution is small in comparison with the streamwise component throughout much of the layer below $z^- \approx 0.3$. However, we cannot assume $V = 0$ if a smooth matching between the inner and outer layers shall be achieved. In this context, we first realize that the velocity deficit $(V^{\alpha_\star} - G^{\alpha_\star})/u_\star$ approaches a Re-independent constant around $C_{V0} = Z_\star \sin\alpha = 6.1$ at the surface; deviations from this constant are only found for the lowest Reynolds numbers which is in accordance with the low-Re correction suggested by Spalart (1989). This constrains the wind veer, and it quantitatively shows that the decreasing wall friction manifest in an increase of $Z_\star$ exactly compensates the decrease of wind turning measured by $\sin\alpha_\star$.

If the difference across the boundary layer is constant (C_{V0}) vs. Re, the averaged gradient $\partial_{z^+} V^{\alpha_\star +}$ of the spanwise velocity component must decrease as $1/\delta^+$ with increasing Re_τ. Hence, it should–at a fixed height–be $V^{\alpha_\star} \propto \left(\delta^+\right)^{-1}$. A profile that agrees with the constraints of the profile at the surface and exploits the dependence of $V^{\alpha_\star}$ on δ^+ is

$$V^{\alpha_\star}\frac{\delta^+}{G} = f_{V,\mathrm{visc}}(z^+) = v_{\mathrm{ref}}\left(\omega_v z^+ - 1 + \exp[-\omega_v z^+]\right), \qquad (14)$$

where v_{ref} controls the magnitude of the profile and ω_v sets the height at which the profile transitions into an approximately linear one. We find excellent agreement with the DNS data for $500 \le \mathrm{Re}_D \le 1600$ below $z^+ \approx 15$ with

$$v_{\mathrm{ref}} = 18.85; \quad \omega_v = 0.2353$$

(cf. Fig. 8b).

For the adjacent surface layer, we find a log-like transition from the quasi-linear profile inner profile around $z^+ = 10$ to a linear profile with increasing Re (Fig. 8b). We model this transition by

$$f_{V,\log}(z^+) = \frac{V_{\log}(z^+)}{G}\delta^+ = a_{\log} + b_{\log}\log z^+ + c_{\log} z^+. \qquad (15)$$

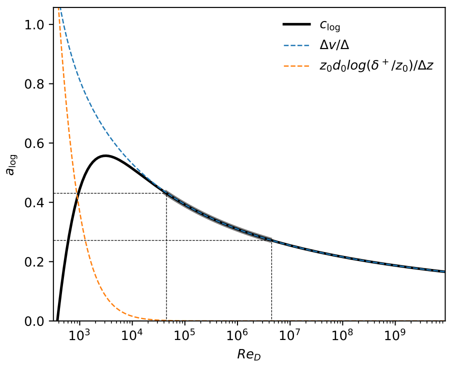

Fig. 9 Coefficients $a_{\rm log}$, $b_{\rm log}$ and $c_{\rm log}$ (cf. Eq. 15) as a function of the viscous Reynolds number Re_D. The approximate range of scale separation relevant for atmospheric application is found in between the dotted lines, where $a_{\rm log} \simeq 0$ and $c_{\rm log} \simeq 0.4$

This surface-layer profile matches the inner (viscous) scaling in vicinity of the surface to the outer (Ekman) scaling above $z^- = 0.3$ when constrained by the viscous profile at the bottom and the Ekman profile at the top:

$$
\begin{aligned}
f_{V,\rm log}(z^+ = 10) &= & f_{V,\rm visc}(z^+ = 10) &=: & v_{10} &\simeq 27.3 & \text{(16a)}\\
\frac{\partial}{\partial z^+}\left[f_{V,\rm log}\right]_{z^+=10} &= & \frac{\partial}{\partial z^+}\left[f_{V,\rm visc}\right]_{z^+=10} &=: & d_{10} &\simeq 4.01 & \text{(16b)}\\
f_{V,\rm log}(z^+ = 0.3\delta^+) &= & V_{\rm ek}^{\alpha_\star}(z^- = 0.3)\delta^+ &=: & & v_{03} & \text{(16c)}
\end{aligned}
$$

where v_{03} is determined by $V_{\rm ek}(0.3)$ and $U_{\rm ek}(0.3)$ and depends on Re. Given the Ekman formulation of the velocity profile introduced in Sec. 4.2, one may express v_{03} using the Ekman profile introduced in Sec. 4.2 together with the approximation for $u_\star(Re)$ found in Eq. (9). While the Re-dependency of $a_{\rm log}$, $b_{\rm log}$, $c_{\rm log}$ is small, it shows up in Fig. 1 where the normalized profiles of spanwise velocity become more convex with increasing Re. We can now quantify this effect by means of the change of $c_{\rm log}$ versus Re which is shown in Fig. 9 (cf. Appendix A.2; $a_{\rm log}$ and $b_{\rm log}$ are then determined by the universal values of v_{10} and d_{10}).

4.5 Matching of the inner and outer layer profiles

The formulations introduced above are continuous across the transition from the inner to the outer layer. However, the requirement of smooth derivatives would over-constrain the velocity profiles and is hence not applied. This can, in particular for low or extremely high Re, cause discontinuity in the derivatives of the velocity profiles around the transition from the inner to the outer layer. To avoid such artificial discontinuity, the profiles are blended by an error-function transition using a blending height $z^-_{blend} = 0.28 - 2.25\sqrt{1/Re_\tau}$ and a transition thickness $z_{\rm trans} = 2$, such that the weighting function $\omega(z^-)$ becomes

$$
\omega(z^-) = \frac{1}{2}\left[\operatorname{erf}\left(z_{\rm trans}\log\frac{z^-}{z^-_{\rm blend}}\right) + 1\right], \tag{17}
$$

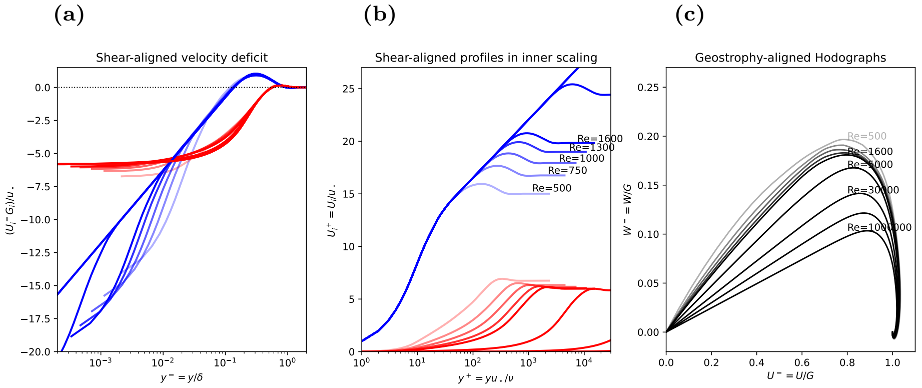

Fig. 10 **(a)** Velocity deficit, **(b)** velocity profile in shear-aligned hodographs and **(c)** hodograph in geostrophy-aligned coordinates. In panels **(a)** and **(b)**, blue lines correspond to the streamwise component and red to the spanwise.

hence $u_{\text{total}} = (1-\omega) \times u_{\text{inner}} + \omega \times u_{\text{outer}}$ and similar for v.

The resulting velocity profiles across the entire boundary layer are shown in inner and outer scaling as well as in hodograph- view in Fig. 10. The shear-aligned velocity deficit is shown in outer scaling highlighting the universality in the outer layer. The logarithmic scaling of the streamwise component is encountered as straight blue lines in panels **(a)** and **(b)** where the extent of the logarithmic range increases with Re towards lower values of z^- and higher values of z^+ depending on the scaling. Importantly, the logarithmic region is widening for increasing Reynolds number – irrespective of the scaling. In this simple inner scaling, the spanwise velocity (which follows a mixed scaling) does not collapse but seems to depend on Re (the collapse is seen in Fig. 8). However, the velocity deficit in outer units becomes approximately universal, also across the inner layer; this reflects the compensation of reduced turning (α) by increased drag ($u_\star$), and is consistent with the theoretical considerations discussed in 4.1.

The spanwise velocity at a fixed height scales approximately as Re_τ^{-1} (Sec. 4.4). However, the fraction of turning that is encountered within the inner layer of the flow amounts to about 1/3 of the total wind veer (Fig. 12a). This is because, in inner units, the inner layer grows as Re_τ which exactly compensates the reduced gradient of spanwise velocity. The hodographs show the well-known Ekman shape with the laminar profile as an outer limit and 'flatter' hodographs, corresponding to less turning, for increasing Reynolds number.

5 Discussion

5.1 Implications for surface-layer scaling

Eq. (14) establishes a universal mixed scaling for the spanwise velocity in the viscous layer: While it requires the vertical coordinate to be expressed in inner units, the velocity itself is normalized by the geostrophic wind, and becomes inversely proportional to the friction Reynolds number $\text{Re}_\tau = \delta^+$ when considered at a fixed height. In vicinity of the surface, such mixed scaling has already been identified

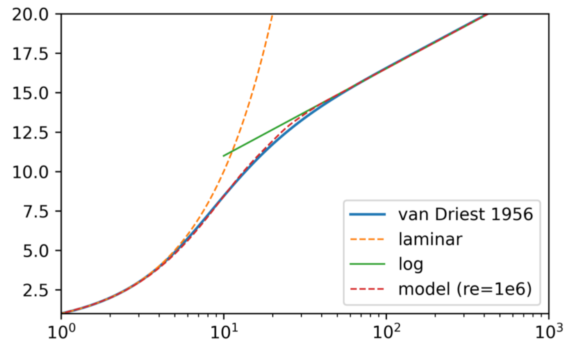

Fig. 11 Near-wall velocity profile according to the van-Driest scaling (blue, solid) in comparison with the present model (red, dashed), the viscous law of the wall (orange dashed), and the logarithmic law (green, solid)

for higher-order statistics in convective flows (Mellado et al. 2016; Li et al. 2018), where large scales leave their signatures in vicinity of the surface. It is important to note here that, while V is a first-order statistic from a statistical perspective, the spanwise velocity is a higher-order correction term from the perspective of similarity theory and from the viewpoint of the channel-flow analogy that is routinely employed in the surface layer. Further, this is consistent with the scaling for the velocity hodograph found in Eq. (11) where the friction velocity also drops out.

In the surface layer, there is not only a mixed scaling–as we had already identified in the viscous layer–, but we cannot find a universal function onto which the profiles of spanwise velocity collapse. This additional degree of freedom reflects the inner–outer matching problem for the spanwise velocity. Rather than giving a universal profile for this region, we resort here to a parametric description of the problem in terms of the function $f_{V,\log}$ determined by the parameters $a_{\log}$, $b_{\log}$, $c_{\log}$ which can be estimated based on the above scaling considerations for any Reynolds number. We note that, once the parameter $a_{\log}$ is known, the parameters $b_{\log}$ and $c_{\log}$ can be estimated solely based on $f_{V,\mathrm{visc}}$, i.e. using the value v_{10} and d_{10} found for the viscous region of the flow. For the range of Reynolds number relevant to geophysical problems ($10^4 \lesssim \mathrm{Re}_D \lesssim 10^6$), the variation of $c_{\log}$ is, however, rather small.

5.2 Comparison with other theories

An alternative approach that considers viscous effects close to the surface is the van-Driest scaling (Van Driest 1956), where an exponential damping of Prandtl's mixing length is considered near the wall to yield

$$\frac{\partial u^+}{\partial z^+} = \frac{2}{1+\sqrt{1+\left(2\kappa z^+\right)^2\left(1-\exp\left[-z^+\right]\right)}}; \tag{18}$$

the spanwise component is zero as no rotational effects are considered. Comparing our proposed formulation for the stream-wise velocity in the inner layer to

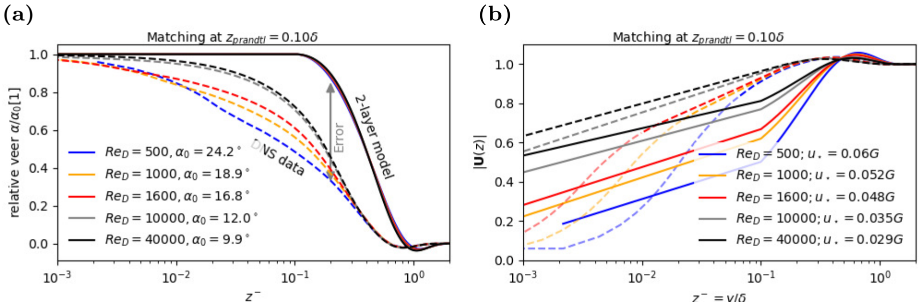

Fig. 12 Comparison of the DNS data (dashed lines) with the two-layer model proposed by Etling (solid lines) for different Reynolds number. Left panel shows the relative wind veer, right panel shows the velocity magnitude. The Etling model is calibrated by the surface veer from the DNS and the roughness parameter is chosen according to the correction factor $\exp \kappa A$ such that the total veer and velocity magnitude agree. Profiles in the buffer layer, defined here as $z^+ < 30$ are shown as opaque dashed lines as the two-layer model does not consider viscous effects.

Van Driest's formulation yields later convergence of the velocity onto the logarithmic profile while, over all, it serves as an excellent model of the streamwise velocity component (Fig. 11): Notable deviations (on the order of few percent) only occur in the region $10 < z^+ < 30$, where the velocity transitions from the linear to the logarithmic profile.

For the higher layers of the ABL, the Ekman spiral is the simplest model available. When employed across the entirety of the ABL, the spiral of a turbulent Ekman layer is flattened with respect to Ekman's laminar solution, which corresponds to a reduction of the veering angle both at the surface and throughout the ABL. We, however, find that a modified version of the Ekman spiral explicitly taking into account the surface boundary condition, is a consistent model and yields excellent agreement with the velocity profiles from DNS (Sec. 4.2).

A two-layer model consolidating both the logarithmic and Ekman layer can be obtained following the arguments by Etling (2008), cf. Emeis (2018). Given a surface veering and a matching height (extent of the logarithmic layer), a formulation for the velocity profile across both the logarithmic and the outer layer is obtained. A comparison using the surface veering based on our model and a matching height of $z_{\text{prandtl}} = 0.05\delta$, which gives better results than the matching height of 0.1δ suggested by Etling (2008), is shown in Fig. 12. The overall shape of velocity magnitude is matched apart from the viscous and buffer layer (cf. Fig. 12b) that is neglected by the two-layer model. However, quantitative departures on the order of 10% occur across the inner layer: it turns out that the non-rotating profile, of the two-layer model in the logarithmic region yields too low overall velocity as the spanwise component contributes to the velocity across the inner layer. Deviations also occur with respect to wind direction; despite the rather low matching height, a substantial fraction of the rotation occurs within the lower part of the ABL and about 20% of the wind veer is not captured by the two-layer model. As the overall veer is given, the non-captured veer close to the surface is then compensated across the logarithmic layer. In the upper part of the boundary layer, both profiles match well.

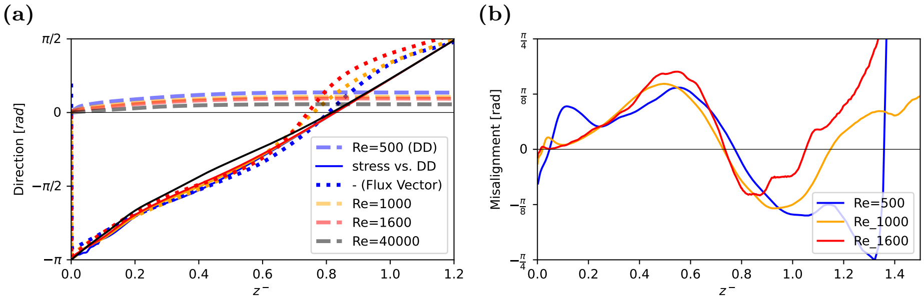

Fig. 13 Panel **(a)** shows the wind direction (DD) as thick dashed lines and the direction of stress relative to DD as thin solid lines, both according to our profile model. The direction of the negative flux vector $(\overline{u'w'}, \overline{v'w'})$ based on DNS data is shown as a dotted line. In panel **(b)**, we plot the misalignment, i.e. the angle, between the flux vector and the shear vector, where the shear vector is defined accordingly as $(\partial_z U, \partial_z V)$.

The interpretation of flux and gradient profiles in terms of the K-theory (cf. Sec. 3, Fig. 2) suggests a certain universality in the inner layer, while a global collapse, i.e. across the boundary layer, is not obtained. While the K-Profiles concern the total stress, a consistent formulation of the turning would also require its partitioning to the individual components, i.e. the orientation of the stress vector $(\overline{u'w'}, \overline{v'w'})$ in the horizontal plane. If K-theory shall be used, this stress vector needs to be anti-parallel to the corresponding stress vector $(\partial_z U, \partial_z V)$. Fig. 13 shows the direction of the velocity, gradient and stress vectors across the boundary layer. It turns out that the negative stress vector with respect to the wind direction and the flux vectors (absolute) have an approximately similar direction. It appears that both rotate by about 270° $(3\pi/2)$ across the boundary layer. Apart from the lower part of the Ekman layer $(0.2 < z^- < 0.7)$, where there is a slight dependence on Re, the direction of stress appears to be universal, which is a consequence of the Ekman profile introduced in Sec. 4.2. However, this implies a misalignment between the flux and the stress on the order of the wind turning, and indeed Fig. 13b shows a misalignment up to $\pi/8$. This is in accordance with the expectation by (Townsend 1976, Chap. 7.18) and prevents the transfer of energy from the mean flow to turbulence at these heights, thus preventing a boundary-layer growth. While the behavior in the inner layer seems to depend on Re, there emerges universality in the misalignment across the outer layer, suggesting that a consideration of misalignment in the context of K-theory is possible when developing formulations for higher-order quantities.

6 Conclusions

We investigate the wind veer and fundamental scaling properties of the velocity profiles in Ekman flow. Based on scaling considerations and direct numerical simulation spanning on decade in external separation from $Re_\Lambda = 1.25 \times 10^5$ to $Re_\Lambda = 1.28 \times 10^6$, we derive a universal formulation for the both horizontal components of the velocity profile in a stationary, smooth Ekman layer. This formulation is consistent with the DNS data and also yields reasonable results at geophysical scale separation; the logarithmic law of the mean velocity is recovered with the well-known limits and deviations towards the surface and Ekman layer. The classic formulation of the Ekman layer, employing the surface boundary condition, is replaced by a modified solution that can be obtained by Ekman's system of governing equations, but using different boundary conditions that are more appropriate of the actual situation encountered in the planetary boundary layer. The three parameters that characterize this boundary condition are estimated based on DNS data.

To quantify the spanwise velocity component consistently across the boundary layer, we derive a universal scaling of the spanwise velocity component in a shear-aligned reference frame. For the *inner layer*, we find the mixed scaling

$$V^{\alpha_\star}/G = \frac{1}{\delta^+} f(z^+) \tag{19}$$

that is, the spanwise velocity normalized by the outer velocity scale is a universal function of the inner height and Friction Reynolds number $Re_\tau = \delta^+$. This scaling is derived here based on scaling considerations, and it is in excellent agreement with the DNS data available. In the outer layer, the spanwise velocity follows outer scaling, consistently with the Ekman model discussed above (Sec. 4.2).

Our results suggest that there is no lower limit of the turning. Hence—despite its very large scale separation / huge Reynolds number—the ABL is not in the 'limit' of high Reynolds number from the perspective of wind veer, but always in a regime where changes in Re impact on the vertical partitioning of rotation.

A Appendices

A.1 Laminar Ekman solution with consideration of inner layer

The following Ekman system is obtained by averaging the Navier–Stokes equations horizontally and over time and neglecting the turbulent transport terms (turbulence can then be considered via the eddy-viscosity concept through variations in the viscosity ν):

$$\begin{pmatrix} \partial_t U \\ \partial_t V \end{pmatrix} = \begin{pmatrix} fV & + \nu\partial_z^2 U \\ -f(U-G) & + \nu\partial_z^2 V \end{pmatrix} \tag{20a}$$

$$\Rightarrow \partial_t(U+iV) = f(V - i(U-G))) + \nu\partial_z^2(U+iV) \tag{20b}$$

In stationary conditions, this system is solved by

$$\hat{u}(z) = U_\infty + e^{-\gamma z}\left[A\cos\gamma z + B\sin\gamma z\right] \tag{20c}$$

$$\hat{v}(z) = V_\infty + e^{-\gamma z}\left[-A\sin\gamma z + B\cos\gamma z\right] \tag{20d}$$

where the constants U_∞, V_∞ set the top boundary condition and A and B set the bottom boundary condition. The most common boundary condition for a surface Ekman layer is $A = U_\infty = G$, $B = 0$, and $V_\infty = 0$. The lower boundary condition, however, neglects the existence of the surface layer, and it appears reasonable to define $A = cG$ where $c < 1$ is a constant that incorporates the increased shear in the surface layer. Given a 'matching height' z_{match} and normalized matching height $\xi = \gamma z_{\mathrm{match}}$ in the upper part of the inner layer, we can match the Ekman profile to the inner layer by letting

$$\begin{aligned} u(z_{\mathrm{match}}) \equiv u_{\mathrm{match}} &= U_\infty + e^{-\xi}\left[A\cos\xi + B\sin\xi\right] \\ v(z_{\mathrm{match}}) \equiv v_{\mathrm{match}} &= V_\infty + e^{-\xi}\left[-A\sin\xi + B\cos\xi\right] \end{aligned} \tag{21a}$$

$$\Rightarrow \begin{pmatrix} u_{\mathrm{match}} - U_\infty \\ v_{\mathrm{match}} - V_\infty \end{pmatrix} = e^{-\xi}\begin{pmatrix} A \\ B \end{pmatrix}\begin{pmatrix} \cos\xi & +\sin\xi \\ -\sin\xi & +\cos\xi \end{pmatrix} \tag{21b}$$

$$\tag{21c}$$

Matching the profile at $\xi = 0$, one obtains $A = \Delta u_{\mathrm{match}}$ and $B = -\Delta w_{\mathrm{match}}$; and when the direction Ox is aligned with the geostrophic wind, we obtain the textbook-case $A = |\mathbf{G}|$ and $B = 0$.

Otherwise, choosing $B \neq 0$ allows to introduce a phase shift of the Ekman rotation with respect to the decay of the wind spiral. However, in our context, the thickness and position of the spiral can already be controlled by the eddy viscosity and an offset in ξ, here we let $B = 0$.

A.2 Matching the spanwise velocity profiles in the inner layer

The spanwise profile in vicinity of the surface is given by $V/G = f_{V,\mathrm{visc}}\delta^+$ with

$$f_{V,\mathrm{visc}} = v_{\mathrm{ref}}\left(\omega_v z^+ - 1 + e^{-\omega_v z^+}\right) \tag{22a}$$

$$f_{V,\log} = a_{\log} + b_{\log}\log z^+ + c_{\log} z^+ \tag{22b}$$

Matching the profiles and gradient $z_0 = 10^+$ and the value at $z_1 = 0.3\delta^+$ yields

$$v_{\mathrm{ref}}\left(\omega_v z_0 + e^{-\omega_v z_0}\right) = v_0 = a_{\log} + b_{\log}\log z_0 + c_{\log} z_0 \tag{23a}$$

$$v_1 = a_{\log} + b_{\log}\log z_1 + c_{\log} z_1 \tag{23b}$$

$$v_{\mathrm{ref}}\omega_z\left(1 - e^{-\omega_z z_0}\right) = d_0 = \frac{b_{\log}}{z_{10}} + c_{\log} \tag{23c}$$

The gradient condition implies $b_{\log} = (d_0 - c_{\log})z_0$, and yields

$$v_0 - z_0 d_0 \log z_0 = a_{\log} + c_{\log}(z_0 - z_0 \log z_0) \tag{24a}$$

$$v_1 - z_0 d_0 \log z_1 = a_{\log} + c_{\log}(z_1 - z_0 \log z_0) \tag{24b}$$

$$\Rightarrow c_{\log} = \frac{\Delta v - z_0 d_0 \log z_1/z_0}{\Delta z} \tag{24c}$$

with $\Delta z = z_1 - z_0$ and $\Delta v = v_1 - v_0$. Then, the coefficient $a_{\log}$ is estimated as

$$a_{\log} = v_0 - z_0 d_0 \log z_0 - \frac{\Delta v - z_0 d_0 \log z_1/z_0}{\Delta z}\left[z_0 - z_0 \log z_0\right]. \tag{24d}$$

We note that $\log(z_1/z_0)/(z_1 - z_0) \to 0$ for large z_1, and as $z_1 = 0.3\delta^+$, this implies that the second term in $c_{\log}$ only plays a role at low and intermediate Re. Then, $a_{\log}$ can be estimated as

$$a_{\log} \simeq v_0 - z_0\left[d_0 \log z_0 - \frac{\Delta v}{\Delta z}(1 - \log z_0)\right] \tag{24e}$$

for large Re.

Acknowledgements This study is funded by the European Commission's 7^{th} Framework Programme through the ERC 2019 Starting Grant trainABL (ID 851374). Simulations were carried out on the German supercomputing systems `hawk` at Höcstleistungsrechenzentrum Stuttgart (Bundesprojekt 44187) and `juwels` at Gauss Centre for supercomputing, Forschungszentrum Jülich (Projects `hku24` and `stadit`). We extend our thanks to Sally Issa for valuable feedback on the manuscript.

Declarations

Author Contributions CA conceived the study, acquired funding, performed the simulation, analysed and plotted the data for this work. CA and HW interpreted the data and compiled the manuscript.

Funding CA is funded by ERC Starting Grant *trainABL* (ID 851374). Open Access funding for this publication through the DEAL agreement.

Data Availability The data is available in long-term repositories and indexed by DOIs as cited in the list of references. Further analysis tools and processed data can be made available upon direct request.

Conflict of Interest The Authors declare no competing interest.

References

Ansorge C (2019) Scale Dependence of Atmosphere–Surface Coupling Through Similarity Theory. Boundary-Layer Meteorol 170(1):1–27, DOI 10.1007/s10546-018-0386-y

Ansorge C (2024a) Direct numerical simulation of turbulent Ekman flow (Re=0500): DOI 10.17169/refubium-42505. DOI 10.17169/refubium-42505

Ansorge C (2024b) Direct numerical simulation of turbulent Ekman flow (Re=1000): DOI 10.17169/refubium-42507. DOI 10.17169/refubium-42507

Ansorge C (2024c) Direct numerical simulation of turbulent Ekman flow (Re=1300): DOI 10.17169/refubium-42508. DOI 10.17169/refubium-42508

Ansorge C (2024d) Direct numerical simulation of turbulent Ekman flow (Re=1600); DOI 10.17169/refubium-42509. DOI 10.17169/refubium-42509

Ansorge C, Mellado JP (2014) Global Intermittency and Collapsing Turbulence in the Stratified Planetary Boundary Layer. Boundary-Layer Meteorol 153(1):89–116, DOI 10.1007/s10546-014-9941-3

Ansorge C, Mellado JP (2016) Analyses of external and global intermittency in the logarithmic layer of Ekman flow. J Fluid Mech 805:611–635, DOI 10.1017/jfm.2016.534

Baars WJ, Marusic I (2020) Data-driven decomposition of the streamwise turbulence kinetic energy in boundary layers. Part 2. Integrated energy and. J Fluid Mech 882:A26, DOI 10.1017/jfm.2019.835

Barenblatt GI (1993) Scaling laws for fully developed turbulent shear flows. Part 1. Basic hypotheses and analysis. J Fluid Mech 248:513–520, DOI 10.1017/S0022112093000874

Barenblatt GI, Goldenfeld N (1995) Does fully developed turbulence exist? Reynolds number independence versus asymptotic covariance. Phys Fluids 7(12):3078–3082, DOI 10/bw2sqs

Blackadar AK, Tennekes H (1968) Asymptotic Similarity in Neutral Barotropic Planetary Boundary Layers. Journal of the Atmospheric Sciences 25:1015–1020, DOI 10.1175/1520-0469(1968)025⟨1015:ASINBP⟩2.0.CO;2

Brown AR, Beljaars ACM, Hersbach H, Hollingsworth A, Miller M, Vasiljevic D (2005) Wind turning across the marine atmospheric boundary layer. Quarterly Journal of the Royal Meteorological Society 131(607):1233–1250, DOI 10/dw2bxz

Calaf M, Meneveau C, Meyers J (2010) Large eddy simulation study of fully developed wind-turbine array boundary layers. Phys Fluids 22(1):015,110, DOI 10/b7gc6v

Coleman GN, Ferziger JH, Spalart PR (1992) Direct Simulation of the Stably Stratified Turbulent Ekman Layer. Journal of Fluid Mechanics 244:677–712, DOI 10.1017/S0022112092003264

da Silva CB, Hunt JC, Eames I, Westerweel J (2014) Interfacial Layers Between Regions of Different Turbulence Intensity. Annu Rev Fluid Mech 46(1):567–590, DOI 10.1146/annurev-fluid-010313-141357

Dimotakis PE (2005) TURBULENT MIXING. Annual Review of Fluid Mechanics 37(1):329–356, DOI 10.1146/annurev.fluid.36.050802.122015

Ekman VW (1905) On the influence of the earth's rotation on ocean currents. Ark Mat Astron Fys, Vol 2 (1905), pp 1-53 2:1–53

Ellison TH (1955) The Ekman spiral. Q J Roy Met Soc 81(350):637–638, DOI 10.1002/qj.49708135025

Emeis S (2018) Wind Energy Meteorology, 2nd edn. Atmospheric Physics for Wind Power Generation, Springer, Heidelberg

Emeis S, Baumann-Stanzer K, Piringer M, Kallistratova M, Kouznetsov R, Yushkov V (2007) Wind and turbulence in the urban boundary layer analysis from acoustic remote sensing data and fit to analytical relations. metz 16(4):393–406, DOI 10.1127/0941-2948/2007/0217

Esau I (2004) Simulation of Ekman Boundary Layers by Large Eddy Model with Dynamic Mixed Subfilter Closure. Environmental Fluid Mechanics 4(3):273–303, DOI 10/b8f3kh

Etling D (2002) Theoretische Meteorologie, 2nd edn. Eine Einführung, Springer-Verlag, Berlin, Heidelberg

Etling D (2008) Theoretische Meteorologie: eine Einführung, 3rd edn. Springer, Berlin Heidelberg

Foken T (2002) Some aspects of the viscous sublayer. metz 11(4):267–272, DOI 10.1127/0941-2948/2002/0011-0267

Foken Th, Kitajgorodskij SA, Kuznecov OA (1978) On the dynamics of the molecular temperature boundary layer above the sea. Boundary-Layer Meteorol 15(3):289–300, DOI 10.1007/BF02652602

Ghannam K, Bou-Zeid E (2021) Baroclinicity and directional shear explain departures from the logarithmic wind profile. Quarterly Journal of the Royal Meteorological Society 147:434–464, DOI 10/gnj6z2

Gryning SE, Batchvarova E, Brümmer B, Jørgensen H, Larsen S (2007) On the extension of the wind profile over homogeneous terrain beyond the surface boundary layer. Boundary-Layer Meteorol 124(2):251–268, DOI 10.1007/s10546-007-9166-9

Högström U (1988) Non-dimensional wind and temperature profiles in the atmospheric surface layer: A re-evaluation. Boundary-Layer Meteorology 42:55–78, DOI 10.1007/BF00119875

Högström U (1996) Review of some basic characteristics of the atmospheric surface layer. Boundary-Layer Meteorology 78(3-4):215–246, DOI 10.1007/BF00120937

Jacobs AF, Van Boxel JH (1988) Changes of the displacement height and roughness length of maize during a growing season. Agricultural Forest Meteorol 42(1):53–62, DOI 10.1016/0168-1923(88)90066-4

Jiang Q, Wang S, Sullivan P (2018) Large-Eddy Simulation Study of Log Laws in a Neutral Ekman Boundary Layer. Journal of the Atmospheric Sciences 75(6):1873–1889, DOI 10.1175/JAS-D-17-0153.1

Jiménez J (2012) Cascades in Wall-Bounded Turbulence. Ann Rev Fluid Mech 44(Volume 44, 2012):27–45, DOI 10.1146/annurev-fluid-120710-101039

Kelly M, Gryning SE (2010) Long-Term Mean Wind Profiles Based on Similarity Theory. Boundary-Layer Meteorol 136(3):377–390, DOI 10.1007/s10546-010-9509-9

Kelly M, Troen I (2016) Probabilistic stability and 'tall' wind profiles: Theory and method for use in wind resource assessment. Wind Energy 19(2):227–241, DOI 10.1002/we.1829

Klein M, Maier RE, Schmidt H (2021) Stochastic modeling of transient neutral and stably-stratified Ekman boundary layers. P A M M 21(1):e202100,146, DOI 10.1002/pamm.202100146

Li Q, Gentine P, Mellado JP, McColl KA (2018) Implications of Nonlocal Transport and Conditionally Averaged Statistics on Monin–Obukhov Similarity Theory and Townsend's Attached Eddy Hypothesis. J Atmos Sci 75(10):3403–3431, DOI 10.1175/JAS-D-17-0301.1

Lindvall J, Svensson G (2019) Wind turning in the atmospheric boundary layer over land. Q J Roy Met Soc 145(724):3074–3088, DOI 10.1002/qj.3605

Mellado J, Ansorge C (2012) Factorization of the Fourier transform of the pressure-Poisson equation using finite differences in colocated grids. Z angew Math Mech 92(5):380–392, DOI 10.1002/zamm.201100078

Mellado JP, van Heerwaarden CC, Garcia JR (2016) Near-Surface Effects of Free Atmosphere Stratification in Free Convection. Boundary-Layer Meteorol 159(1):69–95, DOI 10.1007/s10546-015-0105-x

Mirocha JD, Churchfield MJ, Muñoz-Esparza D, Rai RK, Feng Y, Kosović B, Haupt SE, Brown B, Ennis BL, Draxl C, Sanz Rodrigo J, Shaw WJ, Berg LK, Moriarty PJ, Linn RR, Kotamarthi VR, Balakrishnan R, Cline JW, Robinson MC, Ananthan S (2018) Large-eddy simulation sensitivities to variations of configuration and forcing parameters in canonical boundary-layer flows for wind energy applications. Wind Energy Science 3(2):589–613, DOI 10/gn3nh4

Moin P, Mahesh K (1998) Direct numerical simulation: A tool in turbulence research. Annual Review of Fluid Mechanics 30:539–578, DOI 10.1146/annurev.fluid.30.1.539

Momen M, Bou-Zeid E (2016) Large-Eddy Simulations and Damped-Oscillator Models of the Unsteady Ekman Boundary Layer*. Journal of the Atmospheric Sciences 73(1):25–40, DOI 10.1175/JAS-D-15-0038.1

Momen M, Bou-Zeid E, Parlange MB, Giometto M (2018) Modulation of Mean Wind and Turbulence in the Atmospheric Boundary Layer by Baroclinicity. Journal of the Atmospheric Sciences 75(11):3797–3821, DOI 10/gfmn67

Monin AS (1970) The Atmospheric Boundary Layer. Annual Review of Fluid Mechanics 2:225–250, DOI 10.1146/annurev.fl.02.010170.001301

Monin AS, Yaglom AM (1975) Statistical Fluid Mechanics, Vol. II, Dover Publications on Physics, vol II. Dover Publications, Inc., Mineola

Optis M, Monahan A, Bosveld FC (2014) Moving Beyond Monin-Obukhov Similarity Theory in Modelling Wind-Speed Profiles in the Lower Atmospheric Boundary Layer under Stable Stratification. Boundary-Layer Meteorology 153(3):497–514, DOI 10.1007/s10546-014-9953-z

Rossby CG, Montgomery RB (1935) The layer of frictional influence in wind and ocean currents. Papers in Physical Oceanography and Meteorology III(3):1–101

Sakagami Y, Haas R, Passos JC (2020) Generalized Non-dimensional Wind and Temperature Gradients in the Surface Layer. Boundary-Layer Meteorol 175(3):441–451, DOI 10.1007/s10546-020-00510-3

Spalart PR (1989) Theoretical and numerical study of a three-dimensional turbulent boundary layer. J Fluid Mech 205(-1):319, DOI 10.1017/S0022112089002053

Spalart PR, Coleman GN, Johnstone R (2008) Direct numerical simulation of the Ekman layer: A step in Reynolds number, and cautious support for a log law with a shifted origin. Phys Fluids 20(10):101,507, DOI 10.1063/1.3005858

Spalart PR, Coleman GN, Johnstone R (2009) Retraction: "Direct numerical simulation of the Ekman layer: A step in Reynolds number, and cautious support for a log law with a shifted origin" [Phys. Fluids 20, 101507 (2008)]. Phys Fluids 21(10):109,901, DOI 10.1063/1.3247176

Stoll R, Gibbs JA, Salesky ST, Anderson W, Calaf M (2020) Large-Eddy Simulation of the Atmospheric Boundary Layer. Boundary-Layer Meteorol 177(2-3):541–581, DOI 10/gmbmzw

Svensson G, Holtslag AAM (2009) Analysis of Model Results for the Turning of the Wind and Related Momentum Fluxes in the Stable Boundary Layer. Boundary-Layer Meteorol 132(2):261–277, DOI 10/bwknmt

Tennekes H (1973) A Model for the Dynamics of the Inversion Above a Convective Boundary Layer. Journal of the Atmospheric Sciences

Townsend AA (1976) The Structure of Turbulent Shear Flow, 2nd edn. Cambridge University Press

Van Driest ER (1956) On Turbulent Flow Near a Wall. Journal of the Aeronautical Sciences 23(11):1007–1011, DOI 10.2514/8.3713

Zikanov O, Slinn DN, Dhanak MR (2003) Large-eddy simulations of the wind-induced turbulent Ekman layer. J Fluid Mech 495:343–368, DOI 10/ccbpbw